AIMS Energy, 14(1): 185–211.
DOI: 10.3934/energy.2026008
Received: 20 August 2025
Revised: 03 December 2025
Accepted: 13 January 2026
Published: 06 February 2026

https://www.aimspress.com/journal/energy

Research article

Economic scheduling optimization of microgrids combining generalized energy storage and reward and penalty ladder carbon trading

Qingze Pan[1,2], Haipeng Chen[1,2,*] and Zhiwei Li[3,*]

[1] Key Laboratory of Modern Power System Simulation and Control & Renewable Energy Technology, Ministry of Education, Northeast Electric Power University, Jilin 132012, China
[2] Department of Electrical Engineering, Northeast Electric Power University, Jilin, 132012, China
[3] School of Automation and Engineering, Northeast Electric Power University, Jilin 132012, China

* **Correspondence:** Email: haipeng0704@126.com, zhiwei.li@neepu.edu.cn; Tel: +15944253185, +13844608226.

Abstract: As the connection between the upgraded power grid and users, the microgrid can not only control the output of the local distributed power but also realize a low-carbon transition of users in order to achieve the carbon reduction target. With the aim of reducing operating costs and carbon emissions at the same time, this paper proposes a sustainable economic scheduling strategy combining a ladder-type reward and punishment carbon trading mechanism with generalized energy storage. Initially, the charge and discharge process is analyzed in detail for the energy storage system, and mathematical models relating the actual energy storage system with the virtual energy storage system in the microgrid are established. The composition of the energy supplied to the microgrid and the emission intensity of different power supply sources are analyzed, and a multi-ladder carbon trading mechanism with rewards and penalties is proposed. Subsequently, the typical wind power and photovoltaic power generation cases are simulated by an improved generative adversarial network, which considers the randomness of renewable energy. Eventually, based on MATLAB, a simulation verification is carried out on the proposed scheduling scheme, and the experimental results show that the proposed scheme can effectively reduce operating costs and carbon emissions by 2.03% and 14.08%, respectively, which improves the economy and sustainability of the microgrid.

Keywords: carbon trading; generalized energy storage; sustainable economic scheduling; demand-side flexible resources; microgrid scheduling

1. Introduction

Escalating global CO_2 emissions and energy consumption urgently require the development of a low-carbon economy integrated with society, energy systems, and the environment to achieve green low-carbon development. The power generation structure is undergoing significant change, with increasing emphasis on green innovation [1]. However, the effects of such technological advances on emissions have not yet been properly identified [2]. The inherent features of generation technologies determine how clean power production can be, and both the share of grid-connected renewable generation and the decarbonization of the power sector are vital.

With the promotion of microgrid solutions, the aim is to enhance grid flexibility and foster the regional integration of distributed renewable generation. This initiative is aligned with the structural reform on the supply side of the energy sector. Microgrids will be an indispensable part of the future power system. However, integrating new energy sources into microgrid systems can be very challenging for low-carbon operation due to their uncertainty and volatility. To address this issue, Pan Y et al. [3] proposed an optimization strategy for microgrid clusters incorporating shared hybrid energy storage systems. Their strategy measures the supply-demand state and optimizes system operation by constructing a cost-sharing model to enhance economic performance. Yin L [4] proposed the MHDMOMIA algorithm to optimize microgrid dispatch with the goals of low cost, low carbon emissions, and extended equipment lifetime. By employing a hierarchical distributed structure and multi-modal processing, the method improves economic and environmental performance, providing an effective scheme for microgrids with high renewable penetration. Dong H et al. [5] developed an optimal microgrid scheduling model considering hybrid electric–thermal energy storage. By integrating the advantages of centralized and distributed storage, they constructed a framework in which optimal control of electric–thermal storage reduces investment and maintenance costs while improving system efficiency and resource utilization. Ji BX et al. [6] proposed a staged optimization model with a multi-objective coati optimization algorithm, which can effectively reduce network loss and voltage deviation in active distribution networks with distributed photovoltaics and energy storage, thereby improving operational economy and stability. However, existing microgrid scheduling studies mainly focus on minimizing operation costs while ignoring environmental costs caused during operation.

To develop a microgrid scheduling model that balances economy and low-carbon benefits, the introduction of a carbon trading mechanism provides a new approach for reducing carbon emissions. Li LL et al. [7] proposed a multi-objective artificial hummingbird algorithm for optimizing microgrid energy management systems while considering degradation costs and carbon trading mechanisms, achieving low costs, low carbon emissions, and long equipment lifetime. Zhang J et al. [8] proposed an economic scheduling strategy based on demand-side response and a multi-ladder carbon trading model, establishing an optimization model with the goal of minimizing the total cost of the IES. Gao J et al. [9] proposed an effective scheduling strategy for a combined wind-solar-hydrogen energy system. This strategy implements a laddered carbon trading mechanism within the system and proposes an innovative scheduling model capable of improving the overall cost-effectiveness and operational reliability of the system. Zhan Z et al. [10] evaluated a wind-solar-hydrogen hybrid energy system and proposed a comprehensive optimization scheduling model that considers waste heat recovery from hydrogen fuel cells and a laddered carbon trading strategy, accounting for the coupling of electricity, heat, and hydrogen energy and the complementary characteristics of multiple energy sources over time. Despite the progress in research on low-carbon microgrid operation, these studies

all consider single-carbon trading mechanisms. Consequently, the role of demand-side flexible resources requires further investigation, and how to organically integrate laddered carbon trading and generalized energy storage (GES) remains to be further studied.

Efficient utilization of flexible resources is the key to strengthening the low-carbon microgrid characteristics. Demand-side flexible resources, as the primary source of flexibility, can significantly improve the microgrid's ability to accept distributed energy by increasing their participation rate. Liu L et al. [11] proposed a multi-objective wind-solar-hydrogen hybrid energy supply system optimization method to assess and enhance the utilization of flexible resources, enhancing operational security and responsiveness. Moazzen F et al. [12] introduced a hierarchical microgrid cluster energy management strategy based on a mixed-integer quadratic program, considering battery operation costs and charge-discharge characteristics. By doing so, system reliability and energy usage were enhanced. As energy systems face increasing uncertainty in both supply and demand, and traditional scheduling techniques become inadequate, Zhang Y et al. [13] designed a two-stage joint scheduling scheme for low-carbon operation. By considering supply-demand elasticity and energy heterogeneity, a two-stage optimization model was established to optimize system operating costs by energy demand measurement, index definition, and solution procedures. This improved resource allocation, system flexibility, and economic performance. Previous works have shown that demand-side flexible resources can greatly improve the economic and environmental sustainability of such systems; however, most research has focused on a single type of flexible load. Thermal load controllability is less studied, load characteristic models remain incomplete, and coordination between demand-side flexibility and physical energy storage systems is insufficiently explored.

As an effective way for integrating renewable energy, providing fast response capacity, and reducing operating costs, energy storage units play a crucial role in microgrid systems. Conventional energy storage technologies include electrochemical batteries, pumped hydro storage, thermal storage systems, flywheel storage, hydrogen storage, and gas-based storage. These technologies are typically characterized by dedicated physical devices that store energy during periods of surplus and release it during peak demand, enabling temporal energy shifting. However, the scope of energy storage applications is expanding due to diverse supply-side requirements, increasing penetration of variable renewable energy, and the emergence of demand-side flexibility resources that exhibit a virtual storage effect. This paper introduces the concept of GES, which represents a generic modeling framework encompassing both physical storage technologies and demand-side flexible resources—such as shiftable, transferable, and reducible loads—that can perform energy shifting, capacity provision, or flexibility functions similar to those of storage.

Cui Y et al. [14] reduced total system costs and improved environmental performance by quantifying GES scheduling behavior and nonlinear energy conversion behavior. Zhu D et al. [15] presented a comprehensive optimization model incorporating renewable energy, emissions, GES, and the market, accounting for both demand-side loads and conventional storage. Based on a master–slave game framework and the MADDPG algorithm, Dong Z et al. [16] proposed a hierarchical collaborative optimization model for generalized shared energy storage, integrating physical and virtual storage resources to improve economic performance and dispatch efficiency in distribution networks. Although these studies prove that GES can be used as a stable regulation resource, they have only analyzed the electrical and thermal storage systems, neglecting gas storage. Dong H et al. [17] further showed that accurate modeling through multi-timescale analysis and comprehensive consideration of different energy sources can improve regulation efficiency and expand the energy regulation space.

Still, most existing studies consider only physical energy storage, such as electrical, thermal, and gas storage, and lack integration with demand-side flexible resources. Incorporating both physical storage and demand-side flexibility into the GES can greatly improve the economic performance and carbon reduction capability of microgrids. A comprehensive analysis of the literature, summarized in Table 1, reveals that compared with traditional energy storage, GES offers distinct advantages in terms of composition, regulation, and operation.

Table 1. Comparison of traditional energy storage and GES.

Type	Traditional energy storage	GES
Components	Actual storage	Actual storage and virtual storage
Characteristics	Time-shift, single carrier	Multi-carrier, time, and spatial shift
Functional roles	Peak-shaving, reserve provision	Peak-shaving, reserve provision, flexibility services, demand response

1.1. Research gap

(1) Most studies on load-side flexibility resource scheduling focus on a single type of load-side resource. Research on the controllability, characteristic modeling, and scheduling strategies of multiple load types remains limited. Particularly, significant gaps exist in the controllability of thermal loads and in the development of more refined load characteristic models.

(2) Although several studies have demonstrated the necessity of GES systems for microgrids, most focused on electrical and thermal storage systems; studies on other kinds of energy storage systems, such as gas-based storage, remain limited. In addition, studying the synergistic coordination between GES and load-side flexibility requires further in-depth studies.

(3) Carbon trading mechanisms have been introduced as an effective approach for carbon emission; however, their application to microgrid scheduling optimization has been less explored. Existing studies mostly focus on carbon trading expenditures and emission reduction outcomes while neglecting the influence of laddered carbon trading schemes on microgrid system operation.

1.2. Contributions of this work

(1) Based on the characteristics and controllability of different demand-side flexible assets, this paper proposes customized scheduling methods for different assets, thereby improving microgrid performance and resilience and further enhancing the microgrid's capability in accepting distributed energy resources.

(2) A more comprehensive management model for the GES system is established by integrating different forms of energy storage and load-side flexible resources. While maximizing the utilization of GES, the model enables economically efficient and low-carbon microgrid operation. Further, the synergistic coordination between different forms of energy storage is considered to improve operational efficiency and system reliability.

(3) This paper analyzes the coordinated scheduling of laddered carbon trading and GES, integrates the laddered carbon trading system into microgrid scheduling, and incorporates GES into electrical, thermal, and gas storage configurations. The research objective is to improve the economic and environmental performance of microgrids by implementing a ladder carbon trading mechanism. This mechanism optimizes energy scheduling strategies and reduces carbon emissions.

2. GES model

The share of flexible loads in modern power systems is steadily rising. Their adaptability facilitates temporal energy shifting, akin to actual energy storage units. Therefore, this paper defines GES as an integrated framework encompassing all technologies and resources capable of modulating the temporal and spatial distribution of energy. It includes both physical storage systems and virtual storage resources formed by controllable demand-side flexible loads, such as shiftable, transferable, and reducible loads. Unlike traditional energy storage, which relies solely on actual devices, GES incorporates flexibility-based virtual storage mechanisms that can achieve equivalent energy-shifting functions through demand response. The microgrid system structure containing GES is shown in Figure 1. Detailed parameter settings are provided in Appendix Table 1.

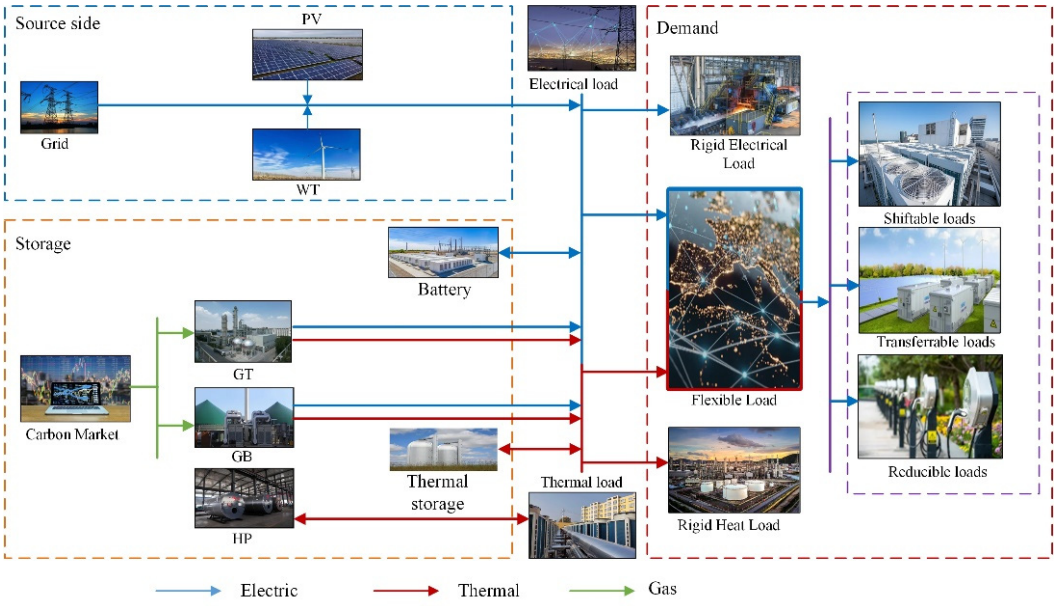

Figure 1. Schematic diagram of the microgrid system structure.

2.1. Actual energy storage model

This paper uses battery and thermal storage tanks as electrical and thermal storage devices. Given the similarities between different real-world energy storage frameworks, a standardized modeling methodology is employed [18] as follows:

$$\begin{cases} 0 \leqslant P_{\mathrm{ESC},t} \leqslant u_{\mathrm{ESC},t} P_{\mathrm{ESC}}^{\max} \\ 0 \leqslant P_{\mathrm{ESD},t} \leqslant u_{\mathrm{ESD},t} P_{\mathrm{ESD}}^{\max} \\ P_{\mathrm{ES},t} = P_{\mathrm{ES},t-1}\left(1-\sigma_{\mathrm{ES}}\right) + \eta_{\mathrm{ESC}} P_{\mathrm{ESC},t} - \dfrac{P_{\mathrm{ESD},t}}{\eta_{\mathrm{ESD}}} \\ u_{\mathrm{ESC},t} \bullet u_{\mathrm{ESD},t} = 0 \\ P_{\mathrm{ES}}^{\min} \leqslant P_{\mathrm{ES},t} \leqslant P_{\mathrm{ES}}^{\max} \end{cases} \tag{1}$$

In the equation, $P_{\mathrm{ESC},t}$ and $P_{\mathrm{ESD},t}$ indicate the energy quantities used during charging and released

during discharging of the actual storage unit, respectively; $u_{\mathrm{ESC},t}$ and $u_{\mathrm{ESD},t}$ indicate the operational status (enabled = 1, disabled = 0) of the electrochemical and electro-thermal storage systems at time *t*; $P_{\mathrm{ESC}}^{\max}$ and $P_{\mathrm{ESD}}^{\max}$ indicate the maximum power tolerance limits for electrochemical energy storage devices and electrothermal energy storage devices; $P_{\mathrm{ES},t}$ denotes the final stored capacity in the energy storage unit at the end of the period; σ_{ES} is the pace at which the actual energy storage device loses self-energy; η_{ESC} and η_{ESD} denote the efficiency rates for charging and discharging in the actual storage system; and $P_{\mathrm{ES}}^{\min}$ and $P_{\mathrm{ES}}^{\max}$ indicate the minimum and maximum limits of the energy state for the energy storage system.

2.2. Virtual energy storage model

Electricity and heat-flexible loads that have the ability to regulate and control the system can be seen as virtual energy storage. Flexible loads have a considerable impact on the energy scheduling of microgrids since they can be controlled in real-time based on power demand. This paper classifies flexible loads into three types according to the differences in their electricity usage characteristics: shiftable, transferable, and reducible loads. Both translatable and shiftable loads can adjust their power supply schedules, but they differ in key aspects: translatable loads must be moved as an intact unit, maintaining a continuous and fixed duration of power consumption, with an unchangeable energy demand during operation, as seen in appliances like washing machines and dishwashers. Compared with translatable loads, shiftable loads are much more flexible and can adjust the power consumption during execution; also, they can interrupt the process without a specified duration, as long as the total energy consumption before and after shifting is the same. EVs are a common type of shiftable load. In a controlled charging plan, charging time and charging power can be adjusted, but the total energy consumption remains the same. Due to the similarity between various virtual energy storage structures, the following modeling method is adopted.

1) Shiftable loads [19]

The pre-scheduling power distribution vector L_{shift}^{*} for translatable load L_{shift} is given by

$$L_{\mathrm{shift}}^{*}=\left(0,\cdots,P_{t_s}^{\mathrm{shift}},P_{t_s+1}^{\mathrm{shift}},\cdots,P_{t_D}^{\mathrm{shift}},\cdots,0\right) \tag{2}$$

In the equation, t_s denotes the initial time interval; t_D indicates the length of time. Assume that the translatable time interval is $[t_{\mathrm{sh}-},t_{\mathrm{sh}+}]$. As the whole interval requires rescheduling, both the starting point and the duration of L_{shift}^{*} must be accounted for. The variable $u_{\mathrm{shift},t}$ indicates the shift condition during a given time slot τ of L_{shift}^{*}; $u_{\mathrm{shift},t}=0$ represents the load L_{shift}^{*} that is not shifted; and P_t^{shift} denotes the power value consumed by the load. Therefore, the collection of initial time slots L_{shift}^{*} is

$$S_{\mathrm{shift}}=[t_{\mathrm{sh}-},t_{\mathrm{sh}+}-t_D+1]\cup\{t_s\} \tag{3}$$

If $\tau=t_s$, the load remains unchanged; if $\tau\in[t_{\mathrm{sh}-},t_{\mathrm{sh}+}-t_D+1]$ and $\tau\neq t_s$ hold, then L_{shift}^{*} transitions from time slot t_s to time slot τ, and the power distribution vector of L_{shift} is

$$L_{\mathrm{shift}}=\left(0,\cdots,P_{t_s}^{\mathrm{shift}},P_{t_s+1}^{\mathrm{shift}},\cdots,P_{t_D}^{\mathrm{shift}},\cdots,0\right) \tag{4}$$

The reimbursement provided to the user following the shift F_{shift} is

$$F_{\text{shift}} = F_{\text{cost}}^{\text{shift}} P_{\text{sum}}^{\text{shift}} \cdot \sum_{t=t_{\text{sh}-}}^{t_{\text{sh}+}-t_D+1} u_{\text{shift},t} \tag{5}$$

In the equation, $F_{\text{cost}}^{\text{shift}}$ indicates the reimbursement rate per unit of shifted power load, and $P_{\text{sum}}^{\text{shift}}$ denotes the overall power consumption of L_{shift}.

2) Transferable loads [20]

Let the time shift interval for the transferable load L_{tran} equal $[t_{\text{tr}-}, t_{tr+}]$. The variable $u_{\text{tran},t}$ represents the transfer status of a specific time period τ of L_{tran}. $u_{\text{tran},t}=1$ represents the power P_{τ}^{tran} that is transferred during the time period τ of L_{tran}, and the transferred power is constrained by the following equation:

$$u_{\text{tran},t} P_{\min}^{\text{tran}} \leqslant P_t^{\text{tran}} \leqslant u_{\text{tran},t} P_{\max}^{\text{tran}} \tag{6}$$

In the equation, $P_{\min}^{\text{tran}}$ and $P_{\max}^{\text{tran}}$ correspond to the lower and upper limits of translatable load power, respectively.

If no restrictions are imposed during load transfer, the load may be shifted to multiple single-time periods, resulting in frequent equipment starts and stops. Therefore, a constraint on the minimum run time of the shifted load must be enforced as follows:

$$\sum_{\tau=t}^{t+T_{\min}^{\tan}-1} u_{\text{tran},t} \geqslant T_{\min}^{\tan}(u_{\text{tran},t} - u_{\text{tran},t-1}) \tag{7}$$

In the equation, $T_{\min}^{\tan}$ represents the shortest allowable continuous run time.

The compensation fee F_{tran} for the user after the transfer is

$$F_{\text{tran}} = F_{\text{cost}}^{\text{tran}} \sum_{t=t_{\text{tr}-}}^{t_{\text{tr}+}} \left(u_{\text{tran},t} P_t^{\text{tran}} \right) \tag{8}$$

In the equation, $F_{\text{cost}}^{\text{tran}}$ signifies the unit compensation rate for transferring power loads.

3) Reducible loads [21]

In contrast to translatable and transferable loads, which maintain unchanged electricity consumption, curtailed loads lead to a reduction in energy usage. The variable $u_{\text{cut},t}$ represents the reduction status of a specific time period τ of the curtailed load L_{cut}, and $u_{\text{cut},t}=1$ represents the reduction of L_{cut} during time period τ. After participating in scheduling, the power during time period τ is

$$P_{\tau}^{\text{cut}} = \left(1 - \theta_{\tau} u_{\text{cut},\tau}\right) P_{\tau}^{\text{cut}^*} \tag{9}$$

In the equation, θ_{τ} denotes the coefficient of load reduction for time slot τ; $\theta_{\tau} \in [0,1]$; $P_{\tau}^{\text{cut}^*}$ indicates the power level at time slot τ prior to L_{cut} starting scheduling. To ensure user satisfaction, limits on the shortest and longest continuous reduction periods and on reduction frequency must be applied.

Restriction on the minimum duration of continuous reduction is as follows:

$$\sum_{t=1}^{t+T_{\min}^{\text{cut}}-1} u_{\text{cut},t} \geqslant T_{\min}^{\text{cut}}(u_{\text{cut},t} - u_{\text{cut},t-1}) \tag{10}$$

The upper bound on continuous reduction duration is

$$\sum_{t=1}^{t+T_{\max}^{\text{cut}}+1} \left(1 - u_{\text{cut},t}\right) \geqslant 1 \tag{11}$$

The reduction frequency constraint [22] is

$$\sum_{t=1}^{24} u_{\text{cut},t} \leqslant N_{\max} \tag{12}$$

$$F_{\text{cut}} = F_{\text{cost}}^{\text{cut}} \sum_{t=1}^{T} u_{\text{cut},t}(P_t^{\text{cut}} - P_t^{\text{cut}^*}) \tag{13}$$

In the equation, $T_{\min}^{\text{cut}}$ denotes the least allowable duration for continuous reduction; $T_{\max}^{\text{cut}}$ represents the upper bound for continuous reduction duration; $N_{\max}$ represents the highest permissible frequency of reduction; F_{cut} denotes the transfer of power load; and $F_{\text{cost}}^{\text{cut}}$ represents the compensation price for the transfer of unit power load.

3. Energy supply equipment model

3.1. GT and WHB model

In a gas turbine (GT) that utilizes natural gas for power production, the correlation between the amount of electricity produced $P_{GT,t}$ and the consumption of natural gas $V_{GT,t}$ are as follows [23]:

$$P_{\text{GT},t} = \frac{V_{\text{GT},t}\eta_{\text{GT}}L_{\text{CH}_4}}{m} u_{\text{GT},t} \tag{14}$$

In the equation, $u_{\text{GT},t}$ represents the operational condition of the GT during the interval t, with a value of 1 (operating) or 0 (shutdown); η_{GT} represents the efficiency with which the GT transforms natural gas into electricity; L_{CH_4} denotes the heat content of natural gas; and m signifies the conversion factor from calorific value to power, established at 3.6.

When the GT engages in scheduled operation, associated operation and maintenance expenses arise. Therefore, the GT's operation and maintenance expenses over period t can be detailed as follows [24]:

$$F_{\text{GT},t} = F_{\text{cost}}^{\text{GT}} P_{\text{GT},t} \tag{15}$$

In the equation, $F_{\text{cost}}^{\text{GT}}$ stands for the coefficient reflecting the GT's operation and maintenance expenses.

The heat the GT produces while generating electricity can be captured by the waste heat boiler (WHB) for subsequent utilization. The heat captured by the WHB, denoted as $E_{t,WHB}$, is as follows [25]:

$$\begin{cases} H_{\mathrm{WHB},t} = \eta_{\mathrm{WHB}} \left(\dfrac{L_{\mathrm{CH_4}} V_{\mathrm{GT},t}}{m} - P_{\mathrm{GT},t} \right) \\ 0 \leqslant H_{\mathrm{WHB},t} \leqslant u_{\mathrm{WHB},t} H_{\mathrm{WHB},t}^{\max} \end{cases} \tag{16}$$

In the equation, η_{WHB} symbolizes the efficiency at which the WHB recovers heat, and $H_{\mathrm{WHB},t}^{\max}$ denotes the peak heat capture capability of the WHB during the interval *t*.

3.2. Gas boiler model

The gas boiler (GB) combusts natural gas to meet thermal load demands. Its model is expressed as follows [26]:

$$H_{\mathrm{GB},t} = \eta_{\mathrm{GB}} V_{\mathrm{GB},t} L_{\mathrm{CH_4}} \tag{17}$$

$$0 \leqslant H_{\mathrm{GB},t} \leqslant u_{\mathrm{GB},t} H_{\mathrm{GB}}^{\max} \tag{18}$$

$$F_{\mathrm{GB},t} = F_{\mathrm{cost}}^{\mathrm{GB}} H_{\mathrm{GB},t} \tag{19}$$

In the equation, $H_{\mathrm{GB},t}$ symbolizes the quantity of heat energy produced by the GB; $V_{\mathrm{GB},t}$ signifies the amount of natural gas utilized; η_{GB} denotes the coefficient of energy conversion efficiency; $H_{\mathrm{GB}}^{\max}$ is the maximum output of the GB; and $F_{\mathrm{cost}}^{\mathrm{GB}}$ is the maintenance cost coefficient for GB.

3.3. Heat pump model

The heat pump (HP) transfers heat from a low temperature reservoir to a higher temperature one, achieving high-efficiency heating. It is modeled as follows [27]:

$$H_{\mathrm{HP},t} = \eta_{\mathrm{HP}} P_{\mathrm{HP},t} \tag{20}$$

$$0 \leq P_{\mathrm{HP},t} \leq P_{\mathrm{HP},t}^{\max} \tag{21}$$

$$F_{\mathrm{HP},t} = F_{\mathrm{cost}}^{\mathrm{HP}} P_{\mathrm{HP},t} \tag{22}$$

where $P_{\mathrm{HP},t}$ represents the electrical energy consumed by the HP, $H_{\mathrm{HP},t}$ denotes the HP's energy conversion efficiency, η_{HP} denotes the HP's operation and maintenance cost coefficient, $P_{\mathrm{HP},t}^{\max}$ denotes the maximum output of the HP, $F_{\mathrm{cost}}^{\mathrm{HP}}$ signifies the operation and maintenance cost coefficient of the HP, and $F_{\mathrm{HP},t}$ signifies the total cost of the HP.

3.4. Renewable energy model

The renewable energy sources primarily consist of distributed wind power and photovoltaic (PV) systems as follows [28]:

$$0 \leq P_{\mathrm{w},t} \leq P_{\mathrm{w},t}^{\max} \tag{23}$$

$$0 \le P_{\mathrm{pv},t} \le P_{\mathrm{pv},t}^{\max} \tag{24}$$

$$F_{\mathrm{W},t} = F_{\mathrm{cost}}^{\mathrm{w}} P_{\mathrm{w},t} \tag{25}$$

$$F_{\mathrm{PV},t} = F_{\mathrm{cost}}^{\mathrm{PV}} P_{\mathrm{pv},t} \tag{26}$$

In the equation, $P_{\mathrm{w},t}^{\max}$ represents the peak wind power output; $P_{\mathrm{p},t}^{\max}$ represents the peak photovoltaic power output power; and $F_{\mathrm{cost}}^{\mathrm{w}}$ and $F_{\mathrm{cost}}^{\mathrm{PV}}$ are the maintenance cost coefficients for wind power and PV systems.

4. RPLCT model

The market-based regulation approach controls total CO_2 emissions by issuing a quota to each emission source. When CO_2 emissions exceed the quota, each source needs to purchase additional permits; when CO_2 emissions are lower than the quota, they can sell the remaining permits. This paper introduces the reward and penalty ladder carbon trading (RPLCT) mechanism in carbon market trading. The CO_2 emissions generated by all devices in each microgrid during operation can be traded in the carbon market. The system is composed of three parts: the carbon allowance model, the real-time emission model, and the RPLCT mechanism.

4.1. Carbon emission quota model

In the microgrids examined here, primary CO_2 sources are grid-purchased electricity, GT units, and GB units. Initial carbon allowances are granted at no cost, with distribution determined by each source's generation capacity. The carbon emission quota model used in this paper is expressed as follows:

$$\begin{cases} E^{\mathrm{MG}} = E^{\mathrm{buy}} + E^{\mathrm{GT}} + E^{\mathrm{GB}} \\ E^{\mathrm{buy}} = \chi_{\mathrm{e}} \sum_{t=1}^{T} P_t^{\mathrm{buy}} \\ E^{\mathrm{GT}} = \chi_{\mathrm{g}} \sum_{t=1}^{T} P_t^{\mathrm{GT}} \\ E^{\mathrm{GB}} = \chi_{\mathrm{g}} \sum_{t=1}^{T} H_t^{\mathrm{GB}} \end{cases} \tag{27}$$

where E^{MG} denotes the aggregate carbon allowance assigned to the microgrid, E^{buy}, E^{GT}, and E^{GB} are the carbon emission quotas for electricity purchased from the grid, GT units, and GB units, respectively; χ_{e} and χ_{g} specify the emission allowances per kilowatt-hour for coal-fired and natural-gas units, set in this paper to 0.798 and 0.486 kg/kWh; and T signifies the scheduling period.

4.2. Actual carbon emission model

The formula for calculating the microgrid's real carbon emissions at time t is:

$$\begin{cases} E^{\mathrm{MG}^*} = E^{\mathrm{buy}^*} + E^{\mathrm{GT}^*} + E^{\mathrm{GB}^*} \\ E^{\mathrm{buy}^*} = \sum_{t=1}^{T} (\alpha_1 P_t^{\mathrm{buy}}) \\ E^{\mathrm{GT}^*} = \sum_{t=1}^{T} (\alpha_2 + \beta_1 P_t^{\mathrm{GT}} + \delta_1 (P_t^{\mathrm{GT}})^2) \\ E^{\mathrm{GB}^*} = \sum_{t=1}^{T} (\alpha_3 + \beta_2 H_t^{\mathrm{GB}} + \delta_2 (H_t^{\mathrm{GB}})^2) \\ C^{\mathrm{MG}} = E^{\mathrm{MG}} - E^{\mathrm{MG}^*} \end{cases} \tag{28}$$

where E^{MG^*} denotes the microgrid's real carbon emissions; E^{buy^*}, E^{GT^*}, and E^{GB^*} represent the actual emissions resulting from grid electricity consumption, GT units, and GB units, respectively; α, β, and δ are the carbon emission factors; and C^{MG} denotes the volume of carbon traded by the microgrid.

4.3. RPLCT cost model

Within the carbon market, the carbon price directly determines trading costs. Carbon pricing schemes fall into two categories: uniform pricing mechanisms and laddered pricing mechanisms. This study defines a reward coefficient derived from the laddered carbon pricing mechanism. Microgrids emitting below their free allowance receive specific rewards and subsidies. The RPLCT carbon trading cost of the micro-network is given in the following equation:

$$F_{\mathrm{CO}_2} = \begin{cases} -v(2+3\gamma)L + v(1+3\gamma)\left(C^{\mathrm{MG}} + 2L\right), C^{\mathrm{MG}} \le -2L \\ -v(1+\gamma)L + v(1+2\gamma)\left(C^{\mathrm{MG}} + L\right), -2L \le C^{\mathrm{MG}} \le -L \\ v(1+\gamma)C^{\mathrm{MG}}, -L \le C^{\mathrm{MG}} \le 0 \\ vC^{\mathrm{MG}}, 0 \le C^{\mathrm{MG}} \le L \\ vL + v(1+\gamma)\left(C^{\mathrm{MG}} - L\right), L \le C^{\mathrm{MG}} \le 2L \\ v(2+\gamma)L + v(1+2\gamma)\left(C^{\mathrm{MG}} - 2L\right), C^{\mathrm{MG}} \ge 2L \end{cases} \tag{29}$$

where F_{CO_2} denotes the microgrid's carbon trading expense, v indicates the foundational carbon price, γ denotes the rate of price increase, and L signifies the span of the emission interval.

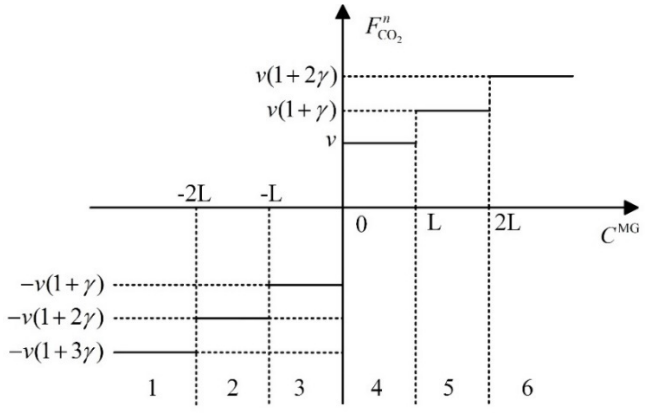

Figure 2. Schematic diagram of the carbon price model for RPLCT.

Figure 2 shows the mathematical model of the carbon price in RPLCT. In this model, $F_{CO_2}^n$ represents the price of unit carbon emissions within the carbon emission interval.

5. Wind and PV scenario generation based on Conditional Wasserstein Generative Adversarial Network with Gradient Penalty (CWGAN-GP)

Figure 3 illustrates that Generative Adversarial Networks (GANs) consist of two separate deep-learning models: a generator and a discriminator. The generator captures the distribution of historical data to transform random noise into synthetic samples, while the discriminator determines if an input originates from real data or from the generator. In adversarial training, the generator seeks to create ever more convincing samples to fool the discriminator, and the discriminator works to correctly distinguish genuine data from generated data. Through this adversarial training process, the authenticity of the generated samples is continuously improved.

To enhance training stability and convergence when generating wind and PV scenarios, this study adopts a CWGAN-GP. Three optimization strategies are applied. First, the Wasserstein distance is used instead of the Jensen-Shannon (JS) divergence to alleviate the gradient-vanishing problem commonly encountered in traditional GAN training. This modification allows a smoother loss landscape and more reliable convergence. Then, a gradient-penalty term is introduced to enforce Lipschitz continuity of the discriminator, which stabilizes the training process and prevents gradient explosion.

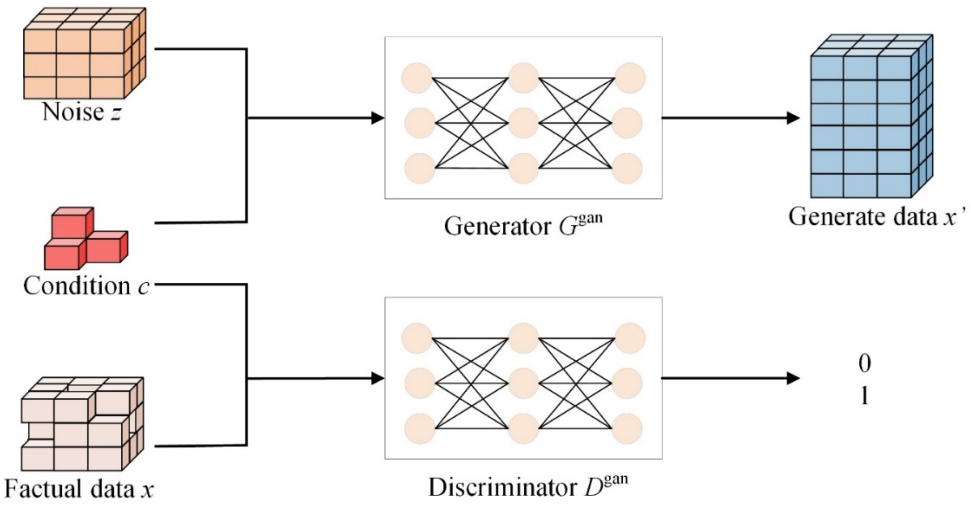

Figure 3. Structure diagram of CWGAN-GP.

The following equations define the loss functions for the generator and the discriminator:

$$L_G = E_{z\sim p_z}[\log(1 - D(G(z)))] \tag{30}$$

$$L_D = -E_{x\sim p_{data}}[\log D(x)] - E_{z\sim p_z}[\log(1 - D(G(z)))] \tag{31}$$

In the formula, E is the expected value of the batch samples; $G(z)$ represents the generated data for wind and PV loads: z is the noise signal; x represents historical data for wind and PV energy; and $D(G(z))$ is the probability that the generated data follows the true distribution.

To address the issue of vanishing gradients that can occur during the training of GANs, the Wasserstein distance is used in place of the JS divergence. The definition of the Wasserstein distance is as follows:

$$W(p_{data}, p_G) = \sup_{\theta_d} E_{x\sim p_{data}(x)}[D(x)] - E_{z\sim p_z(x)}[D(G(z))] \tag{32}$$

In the formula, p_{data} represents the probability distribution of historical wind and PV energy data; P_G represents the probability distribution of the generated wind and PV energy data; $\sup$ represents the least upper bound; and θ_d represents the weights in the discriminator.

Simultaneously, to enable the model to converge faster, we enhance the Lipschitz continuity through a gradient penalty, the expression for which is as follows:

$$\begin{cases} GP = \lambda E[||\nabla D(x')||_2 - 1]^2 \\ x' = \varepsilon x + (1-\varepsilon)G(z), \varepsilon \sim U[0,1] \end{cases} \tag{33}$$

In the formula, λ serves as the weight for the penalty term, and $||\nabla D(x')||_2$ denotes the 2-norm.

In addition, to address the issue of generated data being difficult to control, this paper guides data generation through a conditional variable y. Thus, the objective function of the GANs becomes:

$$\min_G \max_D V(D,G) = E_{x\sim p_{data}(x)}[D(x \mid y)] - E_{z\sim p_z(z)}[D(G(z \mid y))] - \lambda E[||\nabla D(x' \mid y)||_2 - 1]^2 \tag{34}$$

The combined effect of these strategies is reflected in the improved convergence behavior and generation accuracy of the model. As shown in Table 2, the Wasserstein distance between the generated and real distributions under the CWGAN-GP is significantly smaller than that obtained with the baseline GANs. This indicates that the generated samples more accurately capture the statistical features of historical wind and PV data, confirming the effectiveness of the adopted improvements.

Table 2. Comparison of performance among different GAN-based models.

Model	Optimization method	Distance metric used	Convergence stability	Generated data similarity
GAN	JS divergence	-	Unstable	Low similarity
WGAN	Weight clipping; Wasserstein distance	0.092	Moderate stability	Moderate similarity
CWGAN-GP	Gradient penalty; Wasserstein distance	0.046	Stable convergence	High similarity

6. Low-carbon economic scheduling model

6.1. Objective function

The goal is to operate the microgrid economically with low carbon emissions while incorporating demand-side flexibility resources. Subject to each unit's limits, minimize the combined day-ahead operating cost $F_{\cos t}$ and carbon trading cost F_{CO_2} by optimally allocating outputs of controllable units and scheduling demand-side flexibility:

$$\min f = F_{\cos t} + F_{CO_2} \tag{35}$$

$$F_{\cos t} = F_{GT} + F_{GB} + F_{WHB} + F_W + F_{PV} + F_{grid} + F_{HP} + F_{shift} + F_{tran} + F_{cut} + F_{es} \tag{36}$$

In the formula, F_{grid} represents the cost associated with interactions with the power grid, and F_{W} and F_{PV} denote the cost of generating power from renewable energy sources.

6.2. Constraint

$$\begin{cases} P_{\text{GT},t} + P_{\text{W},t} + P_{\text{PV},t} + P_{\text{grid},t} - P_{\text{BAT},t} = P_{\text{Load},t} + P_{\text{HP},t} \\ H_{\text{GB},t} + H_{\text{HP},t} + H_{\text{WHB},t} = H_{\text{Load},t} \end{cases} \tag{37}$$

In the equation, $P_{\text{grid},t}$ denotes the amount of power traded with the electrical grid; $P_{W,t}$ and $P_{PV,t}$ denote the power generated from renewable energy sources; $P_{GT,t}$ denotes the power produced by the GT; $P_{BAT,t}$ denotes the power output from energy storage systems; $H_{\text{HP},t}$ and $H_{GB,t}$ denote the heating power outputs of the HP and GB, respectively; and $P_{\text{load},t}$ and $H_{\text{load},t}$ denote the electrical load demand and the thermal load demand, respectively.

7. Case study analysis

7.1. Case study parameters

This case study is based on a practical microgrid in China. The microgrid optimization scheduling model proposed in this paper is implemented using the forecasted PV and wind resources and the load requirement of the specific region. The microgrid consists of PV units, Wind turbines (WTs), GTs, batteries, and thermal storage tanks. Historical solar irradiance and wind speed data used to generate renewable energy scenarios were obtained from the global hourly meteorological dataset in the National Aeronautics and Space Administration Prediction of Worldwide Energy Resources database. Data representative of the studied microgrid area and covering a full representative year were selected to capture both seasonal and daily changes in available renewable energy. The model incorporates GES, carbon trading, and time-of-use electricity pricing. The scheduling time is 24 h with a scheduling interval of 1 h. The operational parameters of the microgrid are shown in Table 3.

Table 3. Operational parameters of the microgrid.

Type	Power lower limit (kW)	Power upper limit (kW)	Operational cost [USD·(kW·h)$^{-1}$]
Grid	-	-	Time-of-using
WT	0	Predicted value	0.07
PV	0	Predicted value	0.10
GT	0	400	Natural gas price
GB	0	300	Natural gas price

The carbon emission price coefficient is 0.02 USD/kg/t. GT has the maximum output power at 400 kW. The maximum power exchange capacity between the system and the external grid is 300 kW. The above-mentioned trained generator was used to generate the wind and PV output scenarios and to conduct clustering processing. The output data of the wind, PV, and load are shown in Figure 4.

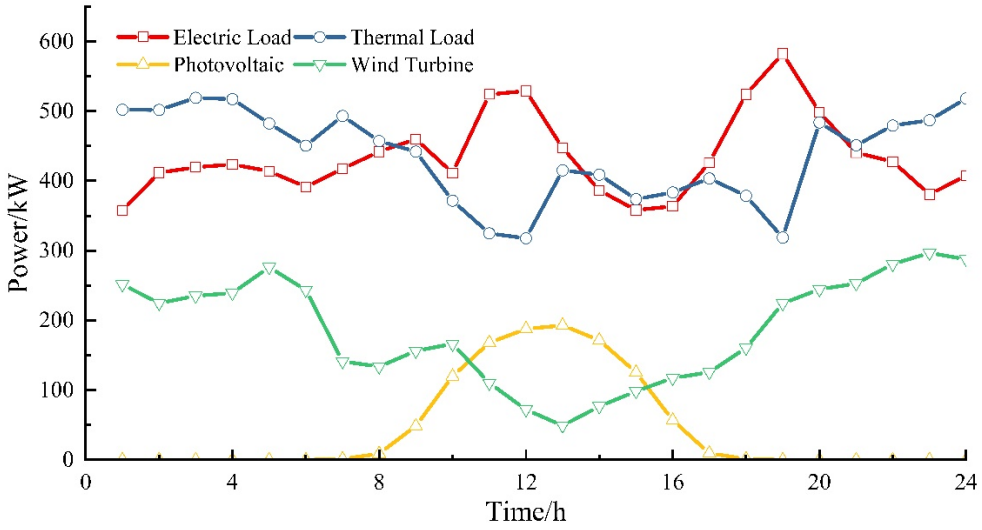

Figure 4. Predicted data for WT, PV output, and electric and thermal load power.

In this paper, MATLAB R2023a software and YALMIP toolbox are used to build the scheduling model, which is solved using Gurobi 9.5.2 solver. In the solver setting, the model optimality MIPGap is set to 1×10^{-4}, and the time is set to 3600 s with branching priorities on the variables of energy storage and flexible load. To guarantee reproducibility, a multi-objective optimization is carried out with a weighted-sum method. With this setting, the model examines how the integrated optimization of flexible loads, real energy storage, and carbon trading affects the microgrid's economy, as summarized in Table 4.

Table 4. Case study scenarios.

Scenarios	RPLCT	GES	
		Actual energy storage	Demand-side flexible resources
Scenario 1	×	×	×
Scenario 2	×	×	√
Scenario 3	×	√	√
Scenario 4	√	×	×
Scenario 5	√	√	√

7.2. Scheduling result analysis for different scenarios

The scheduling schemes were analyzed to assess the financial feasibility and carbon reduction capabilities of the microgrid under five scenarios. Carbon emissions and the optimized scheduling results of each model are presented in Table 5.

Table 3 indicates that Scenario 1 exhibits the most significant carbon emissions out of the five scenarios, with a value of 8494.42 kg. In Scenario 2, which incorporates demand-side flexible resources, carbon emissions are reduced to 8161.28 kg, a decrease of 333.14 kg or 3.92% compared to Scenario 1. Scenario 3, based on demand-side flexible resources, also considers actual energy storage. An energy storage system combines actual energy storage with demand-side flexible resources. By harnessing the attributes of GES, operational expenses are further diminished compared to Scenario 2,

and there is an extra reduction of 1.55% in carbon emissions. In Scenario 4, the addition of the RPLCT mechanism causes total cost to rise marginally by 0.81% relative to Scenario 1, whereas carbon emissions fall by 9.79%. In Scenario 5, GES-enabled peak shaving and valley filling further lowers the total cost compared to Scenario 4. Moreover, the joint operation of the GES and the RPLCT leads to the lowest level of carbon emissions among all scenarios, 4.76% lower than that of the single RPLCT. Meanwhile, Scenario 5 achieves a 2.03% reduction in total operating costs and a 14.08% reduction in total carbon emissions compared with Scenario 1.

Table 5. Carbon emissions and optimized scheduling results under each model.

Model	Total cost (USD)	Carbon emissions (kg)
Scenario 1	956.48	8494.42
Scenario 2	988.03	8161.28
Scenario 3	914.03	8034.67
Scenario 4	964.26	7663.14
Scenario 5	937.05	7298.63

In summary, the rational scheduling of GES, comprehensively considering the actual storage solutions and flexible demand-side assets, can help achieve better low-carbon microgrid performance while ensuring cost-effective scheduling. The implementation of carbon trading can effectively reduce microgrid carbon emissions and enhance its financial and ecological performance.

7.3. The impact of demand-side flexible resources on low-carbon economic scheduling

An optimization scheduling analysis was performed for Scenarios 1 and 2 to verify the impact of demand-side flexible resources on microgrid scheduling. Regarding electricity scheduling, the outputs of renewable energy and GTs in Scenarios 1 and 2 are similar. Scenario 2 leverages demand-side flexibility to schedule the microgrid for economic efficiency and reduced carbon output. To illustrate how the electrical load and thermal load distributions change before and after optimization, Scenario 1 is taken as the scenario before optimization, and Scenario 2 is regarded as the scenario after optimization, as shown in Figures 5 and 6.

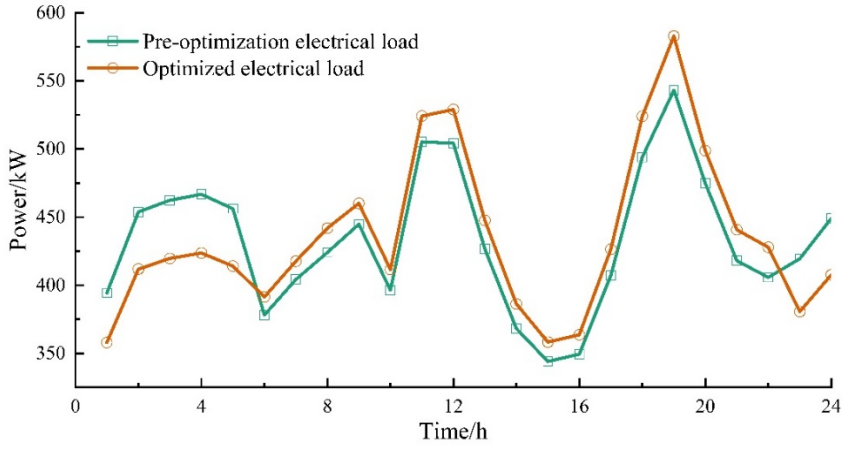

Figure 5. Electrical load curve before and after optimization.

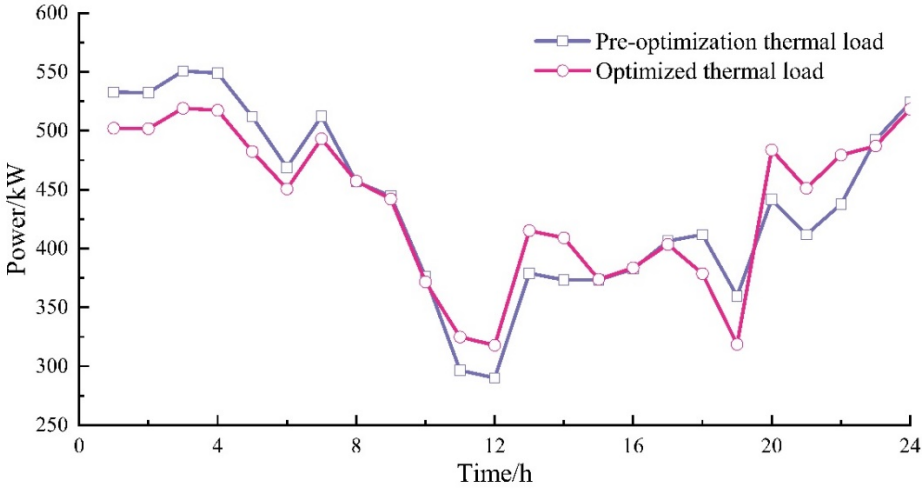

Figure 6. Thermal load curve before and after optimization.

From Figures 5 and 6, it is evident that only during certain intervals, due to the peak shifting and valley filling effects of load-shiftable and load-transferable resources within the demand-side flexible resources, the power output to the grid in Scenario 2 may exceed that of Scenario 1. Additionally, reducing load by demand-side flexible resources decreases the grid output in Scenario 2. Environmentally, cutting grid electricity purchases promotes better clean-energy utilization, lowering both emissions and operating costs.

Figure 7 illustrates the electric power balance under Scenario 2, while Figure 8 illustrates the thermal power balance chart.

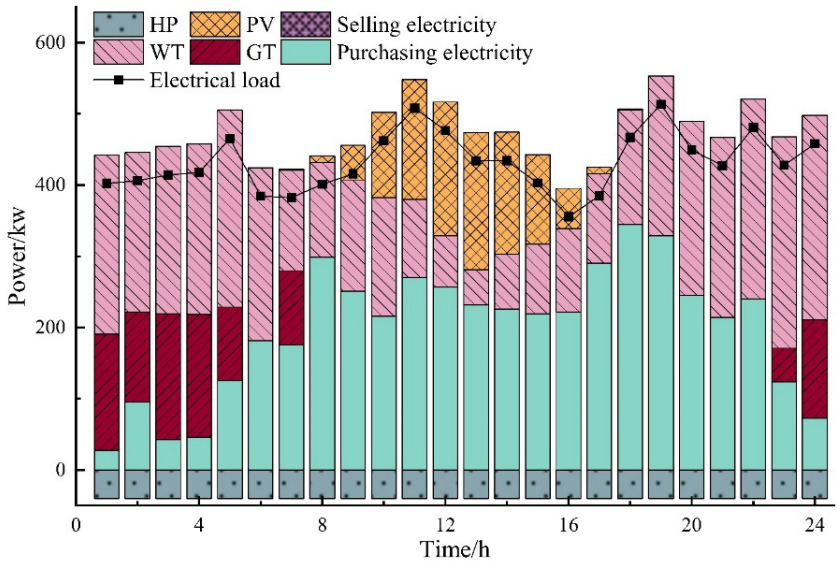

Figure 7. Electric load balance chart for Scenario 2.

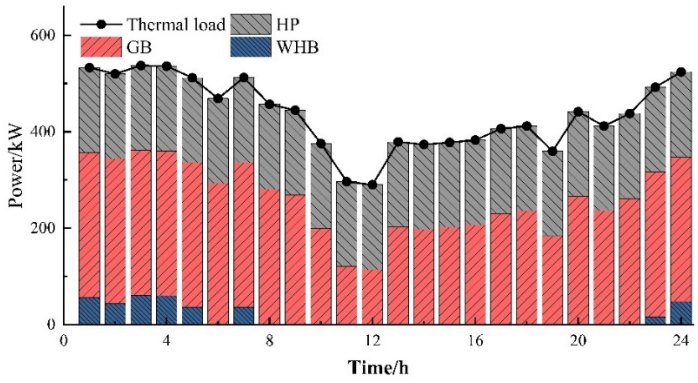

Figure 8. Thermal load balance chart for Scenario 2.

Figure 7 illustrates that from 8:00 to 15:00, there is a plentiful supply of wind and PV resources. Therefore, charging batteries at these times significantly boosts renewable energy utilization. From 16:00 to 24:00, discharging the batteries helps reduce the power supply strain during periods of high electrical demand. Thus, the majority of electricity for electric load is provided with electricity from renewable energy and GT, and only a small amount of electricity needs to be supplemented from the grid. In the scheduling period, the power produced by GT helps to reduce carbon emissions. This strategy reduces the tension on the grid when wind and PV generation are low, and the peak of the load emerges. In contrast to Figure 5, the demand-side flexible electric loads, which can be adjusted and moved, tend to be in a general trend from high consumption time to low and stable time, which is conducive to clean-energy accommodation as well as economical energy distribution management. Furthermore, loads are decreased to varying degrees, with most of the decreased loads aimed at peak electricity use points.

From Figure 8, it can be seen that the GB is operated at full capacity as the scheduling considers minimizing the grid electricity purchased. Thus, the WHB-generated heat mainly serves the thermal load, while the thermal storage and the GB units act as a backup. At low thermal demand periods, i.e., 0:00–4:00, 5:00–9:00, and 22:00–24:00, the storage tanks draw up on the surplus heat from the heat recovery systems for storage, providing it during high thermal demand periods. This process flattens the peaks and fills thermal load valleys. Similar to flexible electric loads on the demand side, compared with Figure 6, the shiftable thermal load is shifted from the evening thermal energy load peak to the valley periods, which also alleviates thermal load stresses in peak demand periods.

In summary, the effective utilization of demand-side flexibility can provide obvious benefits in terms of the microgrid's economic performance and environmental impact. As shown in Table 5, considering flexible demand-side assets in Scenario 2 reduced carbon emissions to 8161.28 kg, a decrease of 3373.14 kg or 3.92% compared with Scenario 1. Therefore, exploiting demand-side flexibility aids in decreasing the overall carbon emissions of the microgrid.

7.4. The impact of GES on low-carbon economic scheduling

As Scenario 3 considers the usage costs of actual energy storage devices and the expenses associated with price-responsive demand in GES, the operational expenditures of the equipment in Scenario 3 are higher than those in Scenario 1. GES, integrating both actual storage solutions and

demand-side adaptability, can significantly smooth microgrid load fluctuations. As a result of this optimization, fuel costs for coal-fired plants are lowered, along with reduced spending on gas procurement.

Figures 9 and 10 illustrate the variations in the electrical load of the microgrid system both before and after incorporating GES. Figures 9 and 10 show that in the 1:00–8:00 and 19:00–24:00 periods, because the output from wind farms exceeds the electrical load, surplus wind power is stored using actual energy storage devices. During these times, price rewards guide users in shifting their electricity usage away from peak periods.

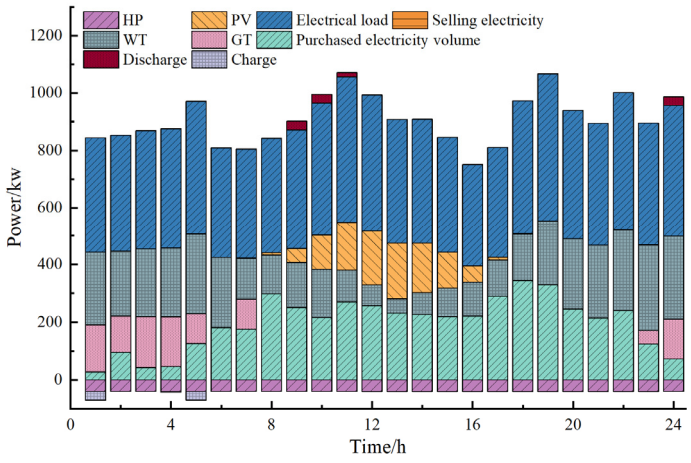

Figure 9. Distribution of demand-side flexible electric load before optimization.

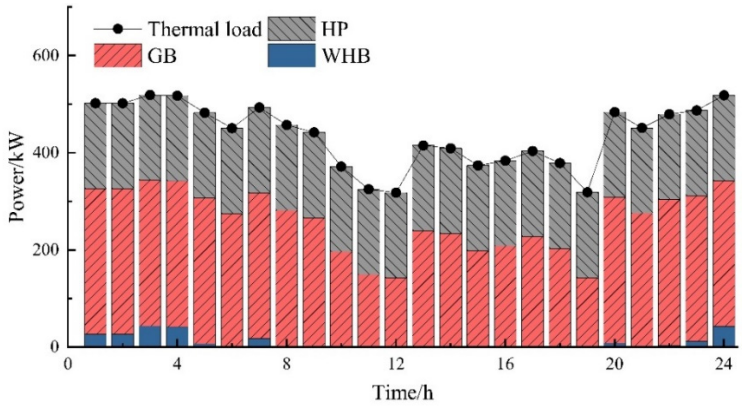

Figure 10. Distribution of demand-side flexible thermal load before optimization.

The thermal load changes are illustrated in Figures 11 and 12. These figures show the changes in both electrical and thermal loads after incorporating GES. To promote wind power consumption via power to hydrogen devices, the thermal load is reduced during the 7:00–13:00 and 16:00–19:00 periods, while it is increased during 1:00–8:00 and 19:00–24:00 periods due to the promotion of wind power consumption. In general, compared with Scenario 1, Scenario 3 decreases the microgrid operation costs by 42.43 USD. Moreover, GES is able to provide support for the microgrid in terms of balancing supply and demand, promoting the utilization of renewables, and enhancing its low carbon capability.

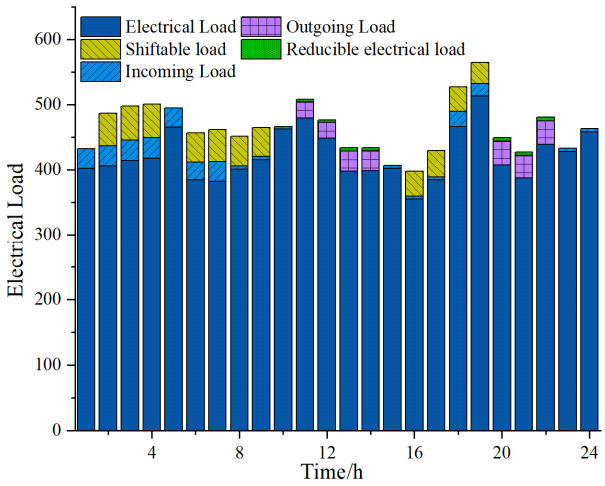

Figure 11. Distribution of demand-side flexible electric load after optimization.

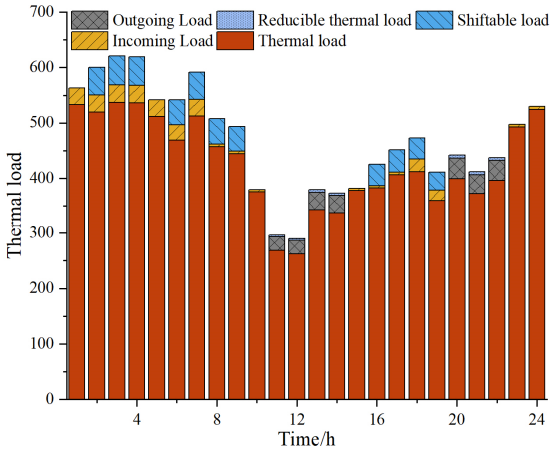

Figure 12. Distribution of demand-side flexible thermal load after optimization.

Figures 13 and 14 show the amount of electricity purchased per period for Scenario 1 and Scenario 3, respectively.

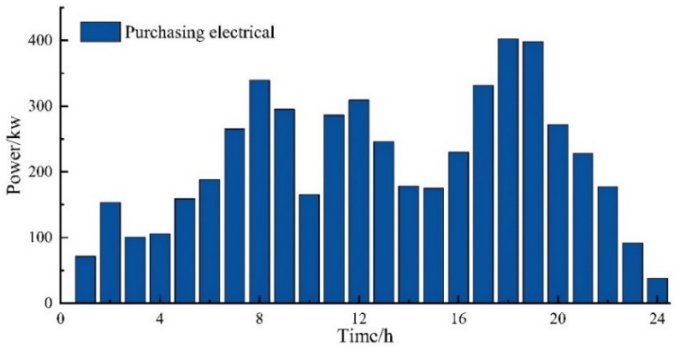

Figure 13. Electricity purchases by period in Scenario 1.

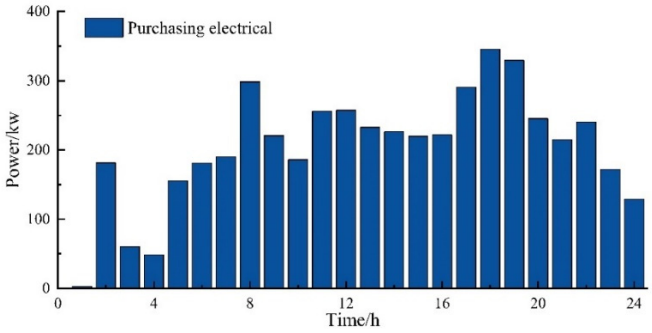

Figure 14. Electricity purchases by period in Scenario 3.

Figures 13 and 14 show that, for Scenario 1, no electricity is sold during operation; as such, the value of purchased electricity is 292.4 kWh higher than that of Scenario 3. For the 15:00–22:00 period, the purchased electricity is higher than that of Scenario 3, and the PV power generation capacity decreases slowly. Scenario 1 is limited by the maximum thermal purchase flow rate, and the operating advantages of thermal units cannot be fully utilized during this period. During peak demand, if Scenario 1 does not have corresponding support from virtual storage and electrical storage, the electricity gap is larger, and procurement prices and total operating costs are higher.

In summary, the difference in operational expenses between Scenarios 2 and 1 increased by 3.29%, while the one between Scenarios 3 and 1 decreased by 4.44%. Carbon emissions decreased by 3.92% between Scenarios 2 and 1 and by 5.41% between Scenarios 3 and 1. The operational expenses and carbon emissions of Scenario 3 decreased further compared to Scenario 2, specifically by 7.49%. Scenario 3 considers GES, such as flexible resources on the demand side and actual energy storage. On the demand side, virtual energy storage can smooth the power consumption curve, performing peak shaving and valley filling.

Most energy storage systems are charged during off-peak rates and discharged during peak rates to achieve an effective time-of-use tariff, in an effective time allocation of various forms of energy. This enhances the system's cost, effectiveness, and adaptability, while supporting economic performance and low carbon in the scheduling of the microgrid.

7.5. The impact of carbon trading mechanisms on microgrid dispatch

In Scenarios 3 and 4, an optimization scheduling analysis was conducted to investigate the impact of the implementation of carbon pricing on microgrid operations. The electric load balance of Scenarios 1 and 4 is illustrated in Figures 15 and 16.

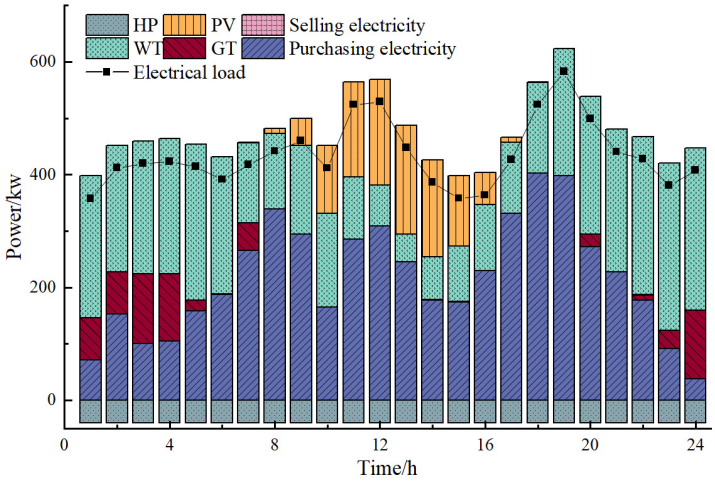

Figure 15. Electric load balance chart for Scenario 1.

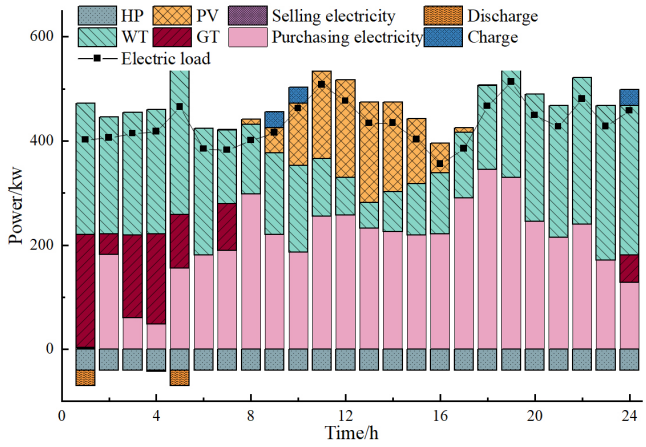

Figure 16. Electric load balance chart for Scenario 4.

Comparing Figures 15 and 16, we observe that in Scenario 1, the curtailment of wind or PV energy is particularly pronounced when electricity prices are low and at a regular time of the day. In Scenario 4, increased usage of renewable energy results in less electricity purchased from the grid when compared to Scenario 1. In Scenario 4, when compared to Scenario 3, actual energy storage and demand-side flexible resources are employed to specifically mitigate peak energy load and energy gaps at low demand, respectively. However, Scenario 4 prioritizes battery charging using renewable energy, showing that carbon trading guides microgrid scheduling in a low-carbon direction.

Scenario 5 introduces a multi-ladder carbon trading mechanism in the carbon trading market. From Figure 17, it can be seen that this scheme has further expanded profit-taking points. Compared with Scenario 1, the total cost decreases by 19.43 USD, accounting for 2.03%. Compared with Scenario 3, it increases by 23 USD, accounting for 2.51%. However, more carbon trading market profits have been obtained, so the carbon emissions are further reduced by 736 kg, accounting for 9.16%. Through a comprehensive comparison, it can be concluded that the overall operating cost of the Scenario 4 system is the lowest, and the scheduling is more flexible.

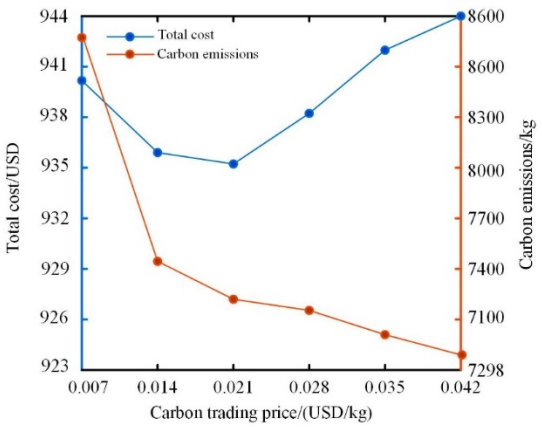

Figure 17. Effects of carbon price volatility on the system's low-carbon performance.

From an environmental perspective, reducing the dependence on grid electricity can more effectively utilize clean energy and thus reduce carbon emissions and operational costs. A carbon trading mechanism is crucial for further reducing emission levels, as it enhances the economic value and environmental benefits of the microgrid.

To compare the convergence efficiency of various scheduling schemes, the following four models with the same boundary conditions are considered: the virtual storage (VS) model, the GES model (actual + virtual storage), the RPLCT model, and the integrated RPLCT + GES model. Figure 18 illustrates the corresponding convergence trajectories.

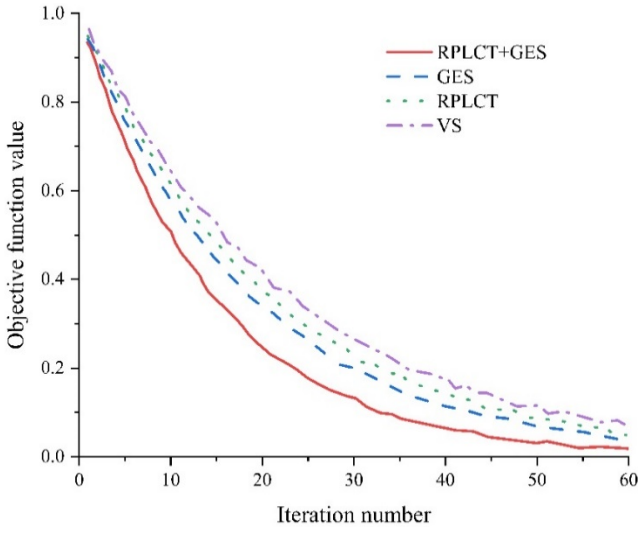

Figure 18. Convergence curves of the four scheduling models.

As illustrated, the RPLCT + GES integrated model has the smoothest and fastest convergence trend, converging in approximately 35 iterations, while the VS, GES, and RPLCT models require 58, 48, and 54 iterations to converge, respectively. The reason for this faster convergence is that the combination of the actual and virtual storages increases the solution space and prevents the models from getting stuck in local optima.

8. Conclusions

To address the challenges of insufficient flexibility and high carbon emissions in microgrids, this study develops a low-carbon economic scheduling approach. The main findings are as follows:

(1) When demand-side flexible resources are incorporated, carbon emissions are reduced to 8161.28 kg, which is 333.14 kg (3.92%) lower than in the case without these resources. This demonstrates that demand-side flexibility scheduling can significantly support the development of a clean energy economy by improving environmental performance while reducing carbon emissions and operational costs.

(2) Compared with the case without GES, the inclusion of both demand-side flexibility and physical energy storage within the GES framework reduces operating costs and carbon emissions by 7.48% and 1.55%, respectively. Demand-side load curves are flattened through peak shaving and valley filling, while energy storage systems are charged during low-price periods and discharged during high-price periods, thereby optimizing temporal energy utilization. GES significantly improves cost-effectiveness, carbon reduction, and operational flexibility of the microgrid.

(3) Compared with a carbon trading mechanism that considers only GES, the microgrid equipped with the RPLCT further reduces carbon emissions by 9.16% on the basis of GES. Moreover, compared with the baseline scenario without any optimization, the total carbon emissions and operating costs are significantly reduced by 14.08% and 2.03%, respectively. The carbon trading system optimizes the microgrid's energy mix, enhancing its economic and environmental benefits.

Use of AI tools declaration

The authors declare they have not used Artificial Intelligence (AI) tools in the creation of this article.

Acknowledgments

This work was supported by the Industrial Technology Research and Development Project of Jilin Province Development and Reform Commission (Award NO. 2024C020-4).

Conflict of interest

The authors declare the following financial interests/personal relationships, which may be considered as potential competing interests: Haipeng Chen reports that financial support was provided by the Industrial Technology Research and Development Project of Jilin Province Development and Reform Commission (Award NO. 2024C020-4). If there are other authors, they declare that they have no known competing financial interests or personal relationships that could have appeared to influence the work reported in this paper.

Author contributions

Qingze Pan: Conceptualization; Haipeng Chen: Supervision; Zhiwei Li: Formal Analysis.

Data availability statement

The data that support the findings of this study are available on request from the corresponding author. The data are not publicly available due to privacy concerns.

Reference

1. Shi H, Chai J, Lu Q, et al. (2022) The impact of China's low-carbon transition on the economy, society, and energy in 2030 based on CO_2 emissions drivers. *Energy* 239: 122336. https://doi.org/10.1016/j.energy.2021.122336
2. Kuang H, Akmal Z, Li F (2022) Measuring the effects of green technology innovations and renewable energy investment for reducing carbon emissions in China. *Renewable Energy* 197: 1–10. https://doi.org/10.1016/j.renene.2022.06.091
3. Pan Y, Ju L, Yang S, et al. (2024) A multi-objective robust optimal dispatch and cost allocation model for microgrids-shared hybrid energy storage system considering flexible ramping capacity. *Appl Energy* 369: 123565. https://doi.org/10.1016/j.apenergy.2024.123565
4. Yin L, Cai Z (2024) Multimodal hierarchical distributed multi-objective moth intelligence algorithm for economic dispatch of power systems. *J Cleaner Prod* 434: 140130. https://doi.org/10.1016/j.jclepro.2023.140130
5. Dong H, Fu Y, Jia Q, et al. (2022) Optimal dispatch of integrated energy microgrid considering hybrid structured electric-thermal energy storage. *Renewable Energy* 199: 628–639. https://doi.org/10.1016/j.renene.2022.09.027
6. Ji BX, Liu HH, Cheng P, et al. (2024) Phased optimization of active distribution networks incorporating distributed photovoltaic storage system: A multi-objective coati optimization algorithm. *J Energy Storage* 91: 112093. https://doi.org/10.1016/j.est.2024.112093
7. Li LL, Ji BX, Li ZT, et al. (2025) Microgrid energy management system with degradation cost and carbon trading mechanism: A multi-objective artificial hummingbird algorithm. *Appl Energy* 378: 124853. https://doi.org/10.1016/j.apenergy.2024.124853
8. Zhang J, Liu Z (2024) Low carbon economic scheduling model for a park integrated energy system considering integrated demand response, ladder-type carbon trading and acceptable utilization of hydrogen. *Energy* 290: 130311. https://doi.org/10.1016/j.energy.2024.130311
9. Gao J, Meng Q, Liu J, et al. (2024) Thermoelectric optimization of integrated energy system considering wind-photovoltaic uncertainty, two-stage power-to-gas, and ladder-type carbon trading. *Renewable Energy* 221: 119806. https://doi.org/10.1016/j.renene.2023.119806
10. Zhan Z, Xu J, Zhang T, et al. (2024) Optimal scheduling of integrated wind-photovoltaic-hydrogen energy system considering hydrogen application and waste heat recovery. *Energy Rep* 11: 3684–3694. https://doi.org/10.1016/j.egyr.2024.03.034
11. Liu L, Zhai R, Hu Y (2023) Multi-objective optimization with advanced exergy analysis of a wind-solar-hydrogen multi-energy supply system. *Appl Energy* 348: 121512. https://doi.org/10.1016/j.apenergy.2023.121512
12. Moazzen F, Hossain MJ (2025) A two-layer strategy for sustainable energy management of microgrid clusters with embedded energy storage system and demand-side flexibility provision. *Appl Energy* 377: 124659. https://doi.org/10.1016/j.apenergy.2024.124659

13. Zhang Y, Zhao H, Qi Z, et al. (2024) A two-stage low-carbon economic coordinated dispatching model for generation-load-storage resources considering flexible supply-demand balance. *Appl Energy* 373: 123981. https://doi.org/10.1016/j.apenergy.2024.123981
14. Cui Y, Wang Y, Xu Y, et al. (2023) Low-carbon economic dispatching of microgrid considering generalized integrated demand response and nonlinear conditions. *Energy Rep* 9: 1606–1620. https://doi.org/10.1016/j.egyr.2022.12.049
15. Zhu D, Cui J, Wang S, et al. (2024) An optimization strategy for intra-park integration trading considering energy storage and carbon emission constraints. *J Cleaner Prod* 447: 141031. https://doi.org/10.1016/j.jclepro.2024.141031
16. Dong Z, Li G, Xie F, et al. (2025) Hierarchical collaborative optimization of generalized shared energy storage system connected to distribution system: A master-slave game based on deep reinforcement learning approach. *Energy Rep*. https://doi.org/10.2139/ssrn.5297368
17. Dong H, Shan Z, Zhou J, et al. (2023) Refined modeling and co-optimization of electric-hydrogen-thermal-gas integrated energy system with hybrid energy storage. *Appl Energy* 351: 121834. https://doi.org/10.1016/j.apenergy.2023.121834
18. Jia J, Li H, Wu D, et al. (2024) Multi-objective optimization study of regional integrated energy systems coupled with renewable energy, energy storage, and inter-station energy sharing. *Renewable Energy* 225: 120328. https://doi.org/10.1016/j.renene.2024.120328
19. Wang C, Fu S, Zhang L, et al. (2023) Optimal control of source-load-storage energy in DC microgrid based on the virtual energy storage system. *Energy Rep* 9: 621–630. https://doi.org/10.1016/j.egyr.2022.12.002
20. Xu Y, Mu Y, Qi H, et al. (2023) Optimal dispatch approach for rural multi-energy supply systems considering virtual energy storage. *Global Energy Interconnect* 6: 675–688. https://doi.org/10.1016/j.gloei.2023.11.002
21. Ma Y, Zhang M, Yang H, et al. (2023) Decentralized and coordinated scheduling model of interconnected multi-microgrid based on virtual energy storage. *Int J Electr Power Energy Syst* 148: 108990. https://doi.org/10.1016/j.ijepes.2023.108990
22. Guo R, Ye H, Zhao Y (2022) Low carbon dispatch of electricity-gas-thermal-storage integrated energy system based on stepped carbon trading. *Energy Rep* 8: 449–455. https://doi.org/10.1016/j.egyr.2022.09.198
23. Kok JBW, Haselhoff EA (2023) Thermodynamic analysis of the thermal and exergetic performance of a mixed gas-steam aero derivative gas turbine engine for power generation. *Heliyon* 9: e18927. https://doi.org/10.1016/j.heliyon.2023.e18927
24. Jia K, Liu C, Li S, et al. (2023) Modeling and optimization of a hybrid renewable energy system integrated with gas turbine and energy storage. *Energy Convers Manage* 279: 116763. https://doi.org/10.1016/j.enconman.2023.116763
25. Wang Y, Li Y, Zhang Y, et al. (2024) Optimized operation of integrated energy systems accounting for synergistic electricity and heat demand response under heat load flexibility. *Appl Therm Eng* 243: 122640. https://doi.org/10.1016/j.applthermaleng.2024.122640
26. Gao L, Fei F, Jia Y, et al. (2024) Optimal dispatching of integrated agricultural energy system considering ladder-type carbon trading mechanism and demand response. *Int J Electr Power Energy Syst* 156: 109693. https://doi.org/10.1016/j.ijepes.2023.109693

27. Zhu G, Gao Y, Liu H (2024) Optimal scheduling of an integrated energy system considering carbon trading mechanism and multi-energy supply uncertainties in a real-time price environment. *Sustainable Energy, Grids Networks* 38: 101351. https://doi.org/10.1016/j.segan.2024.101351
28. Yang M, Shen X, Huang D, et al. (2025) Fluctuation classification and feature factor extraction to forecast very short-term photovoltaic output powers. *CSEE J Power Energy Syst* 11: 661–670. https://doi.org/10.17775/CSEEJPES.2022.03760

Appendix

Table 1. Detailed parameter settings.

Parameter	value	Parameter	value
$P_{\mathrm{ES},t}$	[0 kW, 80 kW]	η_{ESD}	0.93
$P_{\mathrm{ESD},t}$	[0 kW, 80 kW]	$P_{\mathrm{ES}}^{\min}$	20 kWh
$u_{\mathrm{ESC},t}$	[0, 1]	$P_{\mathrm{ES}}^{\max}$	180 kWh
$u_{\mathrm{ESD},t}$	[0, 1]	Δt	1 h
σ_{ES}	0.001	θ_{τ}	[0.05, 0.3]
η_{ESC}	0.93		